Leveraging the Availability of Two Cameras for Illuminant Estimation

Abdelrahman Abdelhamed Abhijith Punnappurath Michael S. Brown
Samsung AI Center – Toronto
{a.abdelhamed,abhijith.p,michael.b1}@samsung.com

Abstract

Most modern smartphones are now equipped with two rear-facing cameras – a main camera for standard imaging and an additional camera to provide wide-angle or telephoto zoom capabilities. In this paper, we leverage the availability of these two cameras for the task of illumination estimation using a small neural network to perform the illumination prediction. Specifically, if the two cameras' sensors have different spectral sensitivities, the two images provide different spectral measurements of the physical scene. A linear 3×3 color transform that maps between these two observations – and that is unique to a given scene illuminant – can be used to train a lightweight neural network comprising no more than 1460 parameters to predict the scene illumination. We demonstrate that this two-camera approach with a lightweight network provides results on par or better than much more complicated illuminant estimation methods operating on a single image. We validate our method's effectiveness through extensive experiments on radiometric data, a quasi-real two-camera dataset we generated from an existing single camera dataset, as well as a new real image dataset that we captured using a smartphone with two rear-facing cameras.

1. Introduction

An overwhelming percentage of consumer photographs are currently captured using smartphone cameras. A recent trend in smartphone imaging system design is to employ two (or more) rear-facing cameras to ameliorate the limitations imposed by the smartphone compact form factor. In most cases, the two rear-facing cameras have different focal lengths and lens configurations to allow the smartphone to deliver DSLR-like optical capabilities (i.e., wide-angle and telephoto). In addition, the two-camera setup has been leveraged for applications such as synthetic bokeh effect [48] and reflection removal [40]. Given the utility of the two-camera configuration, this design trend is likely to continue for the foreseeable future. In this work, we show that the two-camera setup has another benefit, that of improving the accuracy of illuminant estimation.

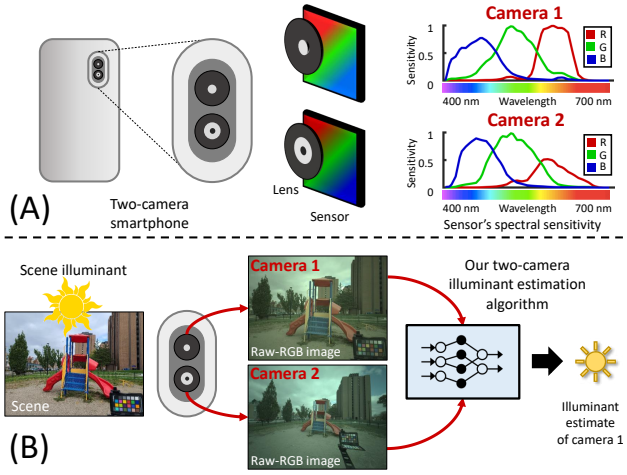

Figure 1: (A) Most modern smartphones use two rear-facing cameras. Typically, the spectral characteristics of these two cameras' sensors are slightly different. (B) Thus, a two-camera system furnishes two different measurements of the scene being imaged. Our proposed two-camera algorithm harnesses this extra information for more accurate and efficient illuminant estimation.

Illuminant estimation is the most critical step for computational color constancy. Color constancy refers to the ability of the human visual system to perceive scene colors as being the same even when observed under different illuminations [39]. Cameras do not innately possess this illumination adaptation ability; the raw-RGB image recorded by the camera sensor has significant color cast due to the scene's illumination. As a result, *computational* color constancy is applied to the camera's raw-RGB sensor image as one of the first steps in the in-camera imaging pipeline to remove this undesirable color cast. The main goal of the camera's auto-white-balance (AWB) module, which is motivated by the concept of computational color constancy, is illuminant estimation. AWB involves estimating the scene illumination in the sensor's raw-RGB color space and then applying a simple 3×3 diagonal matrix computed directly

from the estimated illumination parameters to perform the white-balance correction. Thus, accurate estimation of the scene illumination is crucial to ensuring correct scene colors in the camera image.

We demonstrate that two-camera systems have the potential to provide more accurate illuminant estimation compared to existing single-camera methods. A key insight is that the spectral characteristics of the main camera's sensor are typically different from that of the second camera's. This is due to a variety of reasons. For example, the pitch of the photodiodes and overall resolution of the two sensors are often different to accommodate the different optics associated with each sensor. These differences impact which color filter arrays (CFA) manufacturers can use in the sensor's production process. This results in the two CFAs having different spectral sensitivities to incoming light. While on the surface this may appear to be a disadvantage, differences in the CFA between the two cameras can be corrected for by the later stages of the camera imaging pipeline to ensure the final output colors appear the same (e.g., see [36]). However, for our purpose, the sensors' unprocessed raw images effectively provide *different* spectral measurements of the underlying scene. It is this complementary information that allows us to design a two-camera illumination estimation algorithm as shown in Fig. 1.

Contribution We propose to train a neural network for illuminant estimation that receives as input a 3×3 matrix computed between the two cameras' raw sensor images simultaneously capturing the same scene. Prior work [21] has shown that the color transformation between different spectral samples of the same scene has a unique signature that is related to the scene illumination. This allows the color transformation itself to be used as the feature for illumination estimation. Thus, in contrast to existing single-camera illumination estimation methods that train their deep networks directly on image data, or on image histograms, our network needs to examine only nine parameters in the color transformation matrix. As a result, we can train a very lightweight neural network comprising just 1460 parameters that can be efficiently run on-device in real time. We test our proposed approach extensively with experiments on radiometric data, a quasi-real two-camera dataset we generated from an existing single-camera color constancy dataset [16], and finally on a real two-camera dataset that we captured using a Samsung S20 Ultra smartphone. We compare our technique against several state-of-the-art single-image illuminant estimation methods and demonstrate on par or even improved performance.

2. Related work

We survey works on computational color constancy. These algorithms can be broadly categorized into (1) statistics-based and (2) learning-based methods. While early learning-based approaches used hand-crafted features, more recent works employ deep neural networks.

Statistics-based methods operate using statistics from an image's color distribution and spatial layout to estimate the scene illuminant. Representative examples include gray world [15], general gray world [6], gray edges [46], shades of gray [24], white patch [14], bright pixels [35], and PCA [16]. These methods are fast and easy to implement; however, they make very strong assumptions about scene content and fail in cases where these assumptions do not hold.

Learning-based methods use labelled training data where the ground truth illumination corresponding to each input image is known from physical color charts placed in the scene. In general, learning-based approaches are shown to be more accurate than statistical-based methods. However, learning-based methods usually include many more parameters than statistics-based ones; their number could reach up to tens of millions in some models (e.g., [10]) and they typically have relatively longer training time. Representative learning-based approaches include Bayesian methods [13, 26, 44], gamut-based methods [23, 25, 28], exemplar-based methods [5, 27, 34], and bias-correction methods [4, 18, 19]. While early learning-based methods used hand-crafted features, more recently, deep neural networks (DNN) have demonstrated superior performance [32, 38, 41, 45, 11, 12, 43, 10, 31, 47, 3, 8, 9]. It is important to note that the aforementioned methods are designed to work with a single image captured using three channel sensor. Work by [42] explored the idea of adding an additional color channel, but in the context of resolving scene metamerism. The approach in this paper is based on a pair of images of the same scene captured using a two-camera system.

Our approach is inspired by the chromagenic color constancy technique of Finlayson et al. [22, 21, 17]. The chromagenic approach showed that the parameters of a 3×3 linear transform that relates the color values of a scene captured with different spectral sensitivities are correlated with the scene's illumination. The chromagenic approach used two images captured from the same sensor, but with a color filter applied between image capture; however, two sensors with different spectral sensitivities could also be used. Classification of the scene illumination was performed using a set of pre-selected illuminants via a nearest-neighbour search operation. We build on this method and integrate it into a modern smartphone design with two cameras with different fields of view. Furthermore, we combine it with the power of neural networks to regress over the space of illuminations.

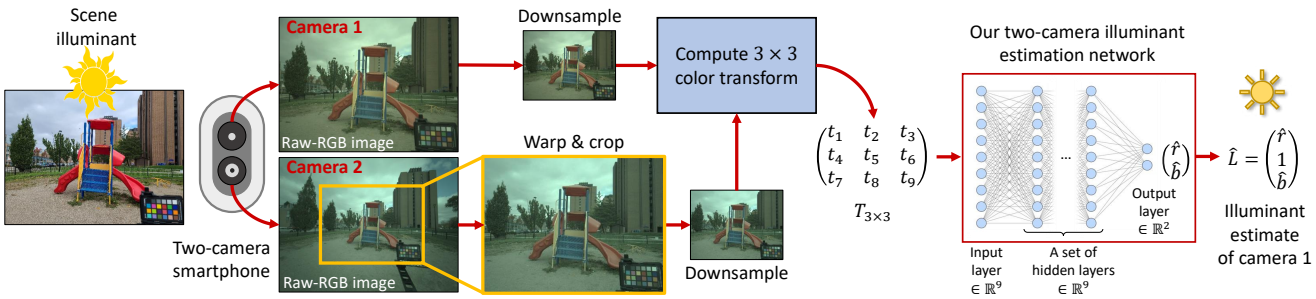

Figure 2: An overview of our proposed two-camera illuminant estimation algorithm. We compute a linear 3×3 transform matrix T that maps the downsampled raw-RGB image from the main camera to the corresponding aligned and downsampled raw-RGB image from the second camera. For a particular scene illuminant, this color transformation T is unique [21]. We feed this mapping T as input to a small lightweight neural network. The network predicts a 2D [R/G B/G] chromaticity value that corresponds to the illuminant estimate of the main camera.

3. Two-camera illuminant estimation

In this section, we describe the various steps of our two-camera illuminant estimation algorithm – spatially aligning the image pairs (Section 3.1); computing color transforms between them (Section 3.2); constructing our two-camera illuminant estimation network (Section 3.3); and augmenting our training data (Section 3.4).

3.1. Image spatial alignment

Our method is based on computing a color transform between a pair of images captured using a two-camera system. These two images usually have different views and need to be registered before computing the color transform. In our experiments on real images, we found that a global homography is sufficient for image alignment. We downsample the images by a factor of six prior to computing the color transform, and this makes our method robust to any small misalignments and slight parallax in the two views. Moreover, since the hardware arrangement of the two cameras does not change for a given device, the homography can be pre-computed and remains fixed for all image pairs from the same device.

3.2. Color transforms for image pairs

Given two raw-RGB images $I_1 \in \mathbb{R}^{n\times3}$ and $I_2 \in \mathbb{R}^{n\times3}$ with n pixels of the same scene captured by two different sensors or cameras, under the same illumination $L \in \mathbb{R}^3$, there exists a linear transformation $T \in \mathbb{R}^{3\times3}$ between the color values of the two images as

$$I_2 \approx I_1\, T, \tag{1}$$

such that T is unique to the scene illumination L [22, 21]. Despite Equation 1 being an approximation, for simplicity, we will use the equality sign instead. We first spatially align the two images using the pre-computed homography, downsample them, and then compute T using the pseudo inverse as follows:

$$T = ({I_1}^T\, I_1)^{-1}\, {I_1}^T\, I_2. \tag{2}$$

3.3. Two-camera illuminant estimation network

Given a dataset of M image pairs

$$\mathcal{I} = \{(I_{1_1}, I_{2_1}), \ldots, (I_{1_M}, I_{2_M})\}, \tag{3}$$

we compute the corresponding color transformations between each pair of images using Equation 2:

$$\mathcal{T} = \{T_1, \ldots, T_M\}. \tag{4}$$

Given the set of corresponding target ground truth illuminants of I_{1_i} (i.e., as measured by the first camera) from each pair

$$\mathcal{L} = \{L_1, \ldots, L_M\}, \tag{5}$$

we can train a neural network $f_\theta : \mathcal{T} \rightarrow \mathcal{L}$, with parameters θ, to model the mapping between the color transforms $\mathcal{T}$ and scene illuminations $\mathcal{L}$. Then, f_θ can be used to predict the scene illumination for the main camera given the color transform between the two images

$$\hat{L} = f_\theta\,(T)\,. \tag{6}$$

Without loss of generality, our method can be trained to predict the illuminant for the second camera as well, using the same color transforms; however, for simplicity, we focus on estimating the illumination for the main camera only. We train our network by minimizing the L_1 loss between the predicted illuminants and the ground truth:

$$\min_\theta \frac{1}{M} \sum_{i=1}^{M} \left| \hat{L}_i - L_i \right|. \tag{7}$$

Our network of choice is lightweight, consisting of a small number (e.g., 2, 5, or 16) of dense layers; each layer has nine neurons only. The total number of parameters

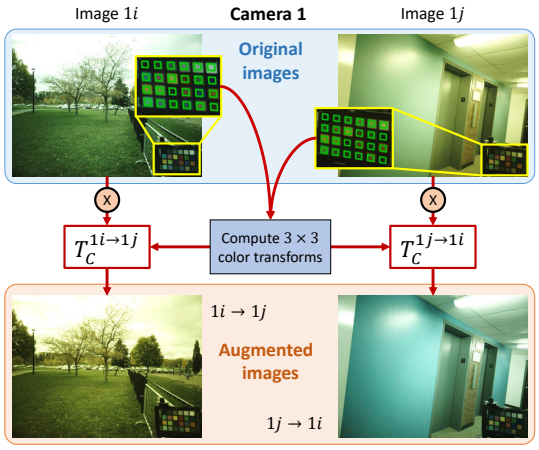

Figure 3: Our image illumination augmentation method. Given a pair of images, we re-illuminate them by each other's illumination based on 3×3 color transformations between their color chart values. This figure shows augmentation of an image pair from one camera only. The corresponding pair of images from the second camera is augmented in the same way. The images shown are in demosaiced raw-RGB format with gamma correction for better visualization.

ranges from 200 for the 2-layer architecture up to 1460 parameters for the 16-layer network. The input to the network is the flattened nine values of the color transform T and the output is two values corresponding to the illumination estimation in the 2D [R/G B/G] chromaticity color space where the green channel's value is always set to 1. An overview of our method is provided in Fig. 2.

3.4. Data augmentation

Due to the lack of large datasets of image pairs captured with two cameras under the same illumination, and to increase the number of training samples and the generalizability of our model, we propose to augment the training images as follows. Given a small dataset of raw-RGB image pairs captured with two cameras and including color rendition charts, we extract the color values of the 24 color chart patches, $C \in \mathbb{R}^{24\times3}$, from each image. Then, we compute an accurate color transformation, $T_C \in \mathbb{R}^{3\times3}$, between each pair of images from the main camera $\left(I_{1_i}, I_{1_j}\right)$ based only on the color chart values from the two images as

$$T_C^{1i\rightarrow1j} = \left(I_{1_i}^T\, I_{1_i}\right)^{-1}\, I_{1_i}^T\, I_{1_j}, \tag{8}$$

and similarly, for image pairs from the second camera $\left(I_{2_i}, I_{2_j}\right)$ as

$$T_C^{2i\rightarrow2j} = \left(I_{2_i}^T\, I_{2_i}\right)^{-1}\, I_{2_i}^T\, I_{2_j}. \tag{9}$$

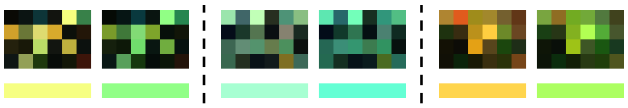

Figure 4: Three samples from our radiometric dataset. Each pair shows images from the main (left) and second (right) cameras. The ground truth illumination colors are presented in the bottom row.

Next, we use this bank of color transformations to augment our images by *re-illuminating* any given pair of images from the two cameras (I_{1_i}, I_{2_i}) to match their colors to any target pair of images $\left(I_{1_j}, I_{2_j}\right)$, as follows:

$$I_{1_{i\rightarrow j}} = I_{1_i}\, T_C^{1i\rightarrow1j}, \tag{10}$$

$$I_{2_{i\rightarrow j}} = I_{2_i}\, T_C^{2i\rightarrow2j}, \tag{11}$$

where $i \rightarrow j$ means re-illuminating image i to match the colors of image j. Using this illuminant augmentation method, we can increase the number of training image pairs from M to M^2. Fig. 3 illustrates an example of re-illuminating a pair of images given another target pair of images.

4. Experiments

To train our two-camera illuminant estimation network, we need a dataset of image pairs of the same scene captured with two different cameras under the same illumination. To our knowledge, there are no publicly available image datasets for color constancy captured using a two-camera system containing labelled ground truth illumination. To validate our method, we first present a synthetic radiometric dataset in Section 4.1. Next, in Section 4.2, we describe how to generate a quasi-real two-camera dataset from an existing single-camera color constancy dataset. Finally, we evaluate our method on a real two-camera image dataset that we captured using a Samsung S20 Ultra smartphone, in Section 4.3.

4.1. Radiometric dataset

To evaluate our method, we generate a synthetic dataset from radiometric data. According to the image formation model, the sensor response is the product of the scene illumination, the surface reflectance, and the sensor's spectral sensitivity, integrated over the visible spectrum. For data generation, we adopt the experimental procedure proposed in [6]. In particular, a scene illuminant and a random set of surface reflectances are selected from a hyperspectral dataset of lights and surfaces [7]. Two different camera sensors with different spectral sensitivity functions are chosen from the camera spectral sensitivity dataset of [33]. The RGB responses for both sensors can then be calculated by

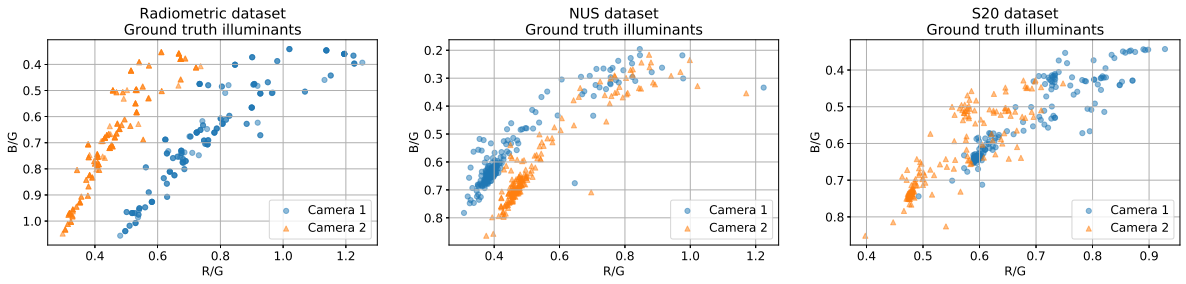

(A) Radiometric dataset (B) Quasi-real NUS dataset (C) Our real dataset

Figure 5: Plots of ground truth illuminants for the two cameras for our (A) radiometric dataset, (B) quasi-real NUS dataset, and (C) real dataset.

simple numerical integration. The response induced by a pure reflector is treated as the corresponding ground truth. The advantage of this procedure is that it is easy to generate a large amount of labelled data to evaluate color constancy algorithms, and arrive at statistically meaningful performance measures.

The reflectance set of [7] consists of 1995 hyperspectral surface reflectance measurements of various natural objects, color charts, and so forth. The dataset of [7] also contains 87 different measured or synthesized illuminant spectra. The camera spectral sensitivity dataset of [33] contains the spectral sensitivity functions for 28 cameras, including mobile phone cameras. We select two sensors from this set to serve as our main camera and the second camera. To generate images, we choose a scene illumination and 24 different surfaces at random, and synthesize the raw-RGB sensor responses for both cameras. We generate thumbnail images of size 32×48 pixels. A few representative examples with associated ground truth are shown in Fig. 4. In total, we generate 18,000 pairs; 10,800 (60%) for training, and 3,600 (20%) each for validation and testing. A plot of the distribution of ground truth illuminants corresponding to the two cameras for 200 random samples is shown in Fig. 5(A). It is evident from the separation between the scatter points corresponding to the two cameras that the same illumination induces very different raw responses in the two sensors owing to the difference in their spectral sensitivity functions.

Method	Mean	Med	B25%	W25%	Q1	Q3
GW [15]	4.09	3.68	1.36	7.51	2.21	5.56
SoG [24]	4.56	4.11	1.51	8.41	2.43	6.21
GE-1 [46]	5.20	4.64	1.65	9.62	2.76	7.18
GE-2 [46]	5.41	4.69	1.72	10.25	2.83	7.37
WGE [29]	4.14	3.25	1.13	8.72	1.82	5.41
PCA [16]	4.55	3.09	1.03	10.67	1.68	5.85
WP [14]	5.49	4.96	1.83	10.02	2.94	7.48
Gamut Pixel [28]	3.68	3.07	1.05	7.30	1.70	5.10
Gamut Edge [28]	6.09	5.34	1.95	11.49	3.15	8.42
Ours (200 params)	2.80	2.20	0.72	5.87	1.19	3.81
Ours (470 params)	**2.65**	**2.00**	**0.64**	**5.72**	**1.07**	**3.61**

Table 1: Angular errors (degrees) on our radiometric dataset. B and W stand for best and worst, while Q1 and Q3 denote the first and third quantile, respectively. Best results are in bold.

For this experiment, we skip the alignment and downsampling steps of Section 3.1 since there is no misalignment, and compute our color transform for each pair from the 24 correspondences. We also omit the data augmentation procedure described in Section 3.4 since we have sufficient training examples. We use the Adam [37] optimizer with a learning rate of 10^{-4}. We train our network for 1 million epochs. The training process takes about 10 hours on a 32 GB nVidia Tesla V100 GPU. Table 1 reports statistics of the angular errors [20] obtained by our method, along with comparisons. The results of comparison methods were computed using open source codes downloaded from [1] or from the authors' webpages. Note that all comparison algorithms are single-image methods, and therefore were given the image from the main camera alone as input. For this experiment, we omit comparisons against deep learning methods since they are typically trained on natural images, whereas our images resemble color checker patches only. From Table 1, we can observe that our method performs better than well-established single-image illuminant estimation methods. Note that although we show illuminant estimation results only for the main camera for simplicity of comparison, our method, without loss of generality, can be used to predict the scene illuminant for the other camera. Please see the supplementary material for more details.

4.2. Quasi-real NUS dataset

In this section, we go a step further beyond synthetic data towards a more real dataset. In particular, we describe a procedure to generate a *quasi-real* two-camera dataset from an existing single-camera color constancy dataset. Towards this goal, we select the NUS [16] dataset, which has images

Figure 6: Sample matched pairs from the NUS dataset that we use to generate our quasi-real dataset.

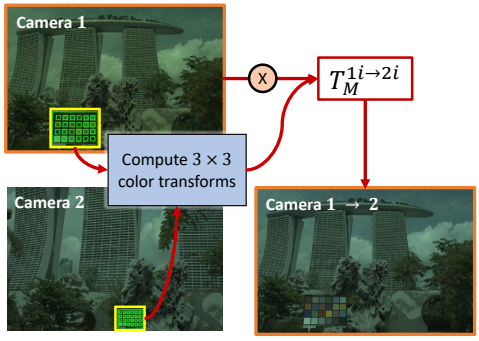

Figure 7: Our method for generating spatially-aligned two-camera image pairs from the NUS dataset. A color transform is used to map the image's colors from one camera to the other.

of the same scene mostly under the same illumination captured using different cameras. We choose the Nikon D5200 as the main camera while the Canon 1Ds Mark III serves as the second camera. We select only those images where the two cameras are observing the same scene with no visible changes in the illumination. After filtering, we obtain 195 matched pairs from the two cameras. All images in the NUS dataset have a Macbeth color chart placed in the scene. The ground truth scene illumination can be obtained from the achromatic patches in the color chart. A plot of the ground truth illuminants for the 195 images from the two cameras is shown in the plot of Fig. 5(B), and it can be observed that the two sensors record different measurements for the same illumination. A few representative examples of matched image pairs from the two cameras are shown in Fig. 6. Notice that some pairs have a significant change in viewpoint although the scene is the same. Therefore, we preprocess the data to generate our quasi-real dataset, as described next.

For each image pair (I_{1i}, I_{2i}) from the two cameras, we first compute an accurate 3×3 transform $T_M^{1i\to 2i}$ that maps the raw-RGB image from the main camera to the second camera using *only* the 24 correspondences from the color checker patches. Next, we apply this color transform on the main camera image to synthesize a new second camera image. This procedure is shown in Fig. 7. These two spatially aligned images constitute a pair in our quasi-real dataset.

We use a standard three-fold cross validation protocol to evaluate performance. For learning-based methods, including our own approach, we augment the training folds using the procedure described in Section 3.4. Testing is performed on the original unaugmented set. In particular, for each image pair, we generate another 99 randomly re-illuminated image pairs to obtain a total of 19500 pairs. The color chart is then masked out in all training, validation, and testing images. The results of our method, along with comparisons, are presented in Table 2. In addition to several classical methods, we also test against the recent learning approaches of [3, 10, 32, 9]. For all four learning methods, publicly available implementations provided by the authors were used to report results. The method of [3] is sensor-independent, and does not require re-training. The quasi unsupervised color constancy algorithm of [10], while inherently sensor-agnostic, can be fine-tuned if annotated training data is available. In Table 2, we report results both without and with fine-tuning, using the pre-trained models made available by the authors. For the fine-tuned result, we selected the appropriate pre-trained model for testing based on the three-fold partitioning indices of the NUS dataset used by the authors. For FC4 [32], we trained the model from

Method	Mean	Med	B25%	W25%	Q1	Q3
GW [15]	4.43	3.42	0.90	9.82	1.54	6.11
SoG [24]	3.31	2.63	0.70	7.20	1.18	4.17
GE-1 [46]	4.49	3.03	0.87	10.38	1.40	6.34
GE-2 [46]	4.99	3.28	0.94	11.83	1.54	6.65
WGE [29]	5.77	3.11	0.77	14.75	1.38	7.89
PCA [16]	4.01	2.68	0.69	9.20	1.22	6.07
WP [14]	4.49	3.47	0.93	9.99	1.42	6.09
Gamut Pixel [28]	5.99	3.70	0.90	14.95	1.41	8.65
Gamut Edge [28]	4.99	3.38	0.85	11.63	1.72	7.22
CM [18]	2.80	2.09	0.66	6.12	1.21	3.67
Homography [19] (SoG)	2.70	1.95	0.69	5.88	1.06	3.71
Homography [19] (PCA)	2.97	2.16	0.72	6.47	1.14	4.22
APAP [4] (GW)	2.64	2.00	0.60	5.99	1.02	3.26
APAP [4] (SoG)	2.49	1.75	0.60	5.61	0.88	3.14
APAP [4] (PCA)	2.77	1.83	0.60	6.45	0.94	3.49
SIIE [3]	2.04	1.55	0.51	4.41	0.80	2.80
Quasi U CC [10]	3.57	2.77	0.62	8.04	1.09	5.06
Quasi U CC finetuned [10]	2.68	1.72	0.57	6.25	0.98	3.67
FC4 [32]	2.65	2.06	0.67	5.69	1.12	3.49
FFCC [9]	2.44	1.50	0.40	5.87	0.75	3.19
Ours (200 params)	2.39	1.44	0.46	5.95	0.81	2.81
Ours (470 params)	1.91	1.24	0.36	4.78	0.62	2.22
Ours (1460 params)	**1.69**	**1.09**	**0.37**	**4.02**	**0.59**	**2.02**

Table 2: Angular errors (degrees) on the main camera from our quasi-real NUS [16] dataset. Best results are in bold.

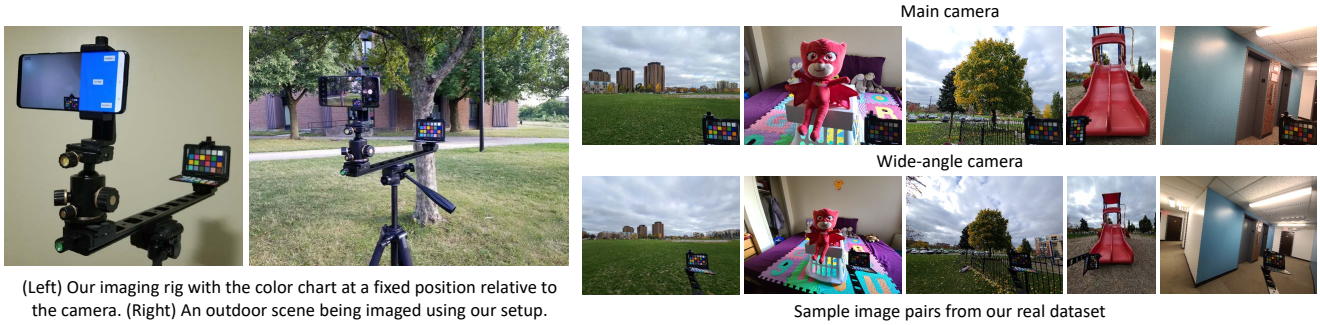

Figure 8: Our data capture setup and representative examples from our dataset. Note that while illuminant estimation is performed on the raw-RGB sensor image, we show here the corresponding sRGB images to aid visualization.

scratch using the hyperparameters recommended by the authors. For FFCC [9], the hyperparameters were carefully tuned to achieve the best performance. In the literature, FC4 and FFCC are currently the best-performing methods across all color constancy datasets, including NUS. It can be observed that our model with 1460 parameters outperforms both FC4 and FFCC, as well as other competitors.

4.3. S20 real-image dataset

The final step in our evaluation is to collect and test on a real dataset of image pairs captured using a two-camera system. Towards this goal, we examined various recent smartphones with two rear-facing cameras. Our method requires access to the raw-RGB images from both cameras. The Samsung S20 Ultra is one smartphone we found that has the desired camera configuration and allows saving to the raw format. The S20 Ultra is equipped with a wide-angle rear-facing camera that provides a larger field of view than the main camera. The two camera sensors are different: the main camera is a Samsung HM1 sensor (108 MP, 3x3 Nonacell, $0.8\mu m$ pitch), while the second camera is a Samsung S5K2L3SX sensor (12 MP, $1.4\mu m$ pitch). While we do not have access to the sensors' CFA spectral sensitivities, it is easy to verify the CFAs are different by observing a color checker chart under the same controlled illumination and plotting the responses. See Fig. S1 of supplemental for more details on how we validate that the spectral sensitivities of the two cameras are different. We used image pairs from the main camera and the wide-angle camera for our experiments. We developed a simple Android application with the aid of the Camera2 API [30] to save the raw-DNG files from both cameras with a single button press. To obtain the ground truth, a Macbeth color chart was placed in every scene. For ease of ground truth labelling, we used a custom rig (see Fig. 8) that allows the color chart to be placed at a fixed position relative to the camera. This ensures that the color chart always occupies a fixed spatial location in the captured images. We collected a total of 156 image pairs, spanning a diverse range of lighting conditions and scene content. Some representative examples from our dataset are shown in Fig. 8. Fig. 5(C) shows a plot of the distribution of the ground truth illuminants for the two cameras. It is clear from the spread in the distribution that our working assumption of two-camera systems having different spectral profiles can likely hold true on real data.

As a preprocessing step, the raw-DNG images from our dataset were demosaiced and the black level was adjusted. The ground truth illumination was also extracted from the color chart. Since the field of view is different between the two cameras, before downsampling, we registered the images using a fixed pre-computed homography as described

Method	Mean	Med	B25%	W25%	Q1	Q3
GW [15]	3.25	2.55	0.90	6.94	1.46	3.73
SoG [24]	3.07	2.03	0.62	7.33	0.98	4.16
GE-1 [46]	4.79	3.91	0.94	10.72	1.49	6.35
GE-2 [46]	5.23	3.96	0.95	11.74	1.57	7.76
WGE [29]	6.17	4.76	0.85	14.17	1.50	9.79
PCA [16]	4.56	3.35	0.85	10.50	1.32	6.42
WP [14]	3.24	2.30	0.56	7.48	1.03	4.16
Gamut Pixel [28]	6.81	5.62	0.97	14.20	1.61	10.29
Gamut Edge [28]	5.00	3.60	0.94	11.20	1.46	6.58
CM [18]	3.51	2.64	0.66	7.64	1.25	4.83
Homography [19] (SoG)	3.43	2.38	0.46	7.93	1.13	4.90
Homography [19] (PCA)	4.35	3.12	0.58	10.09	1.05	6.35
APAP [4] (GW)	4.21	2.32	0.53	11.34	0.88	4.81
APAP [4] (SoG)	3.46	2.29	0.39	8.53	0.73	5.18
APAP [4] (PCA)	3.96	2.77	0.47	9.14	0.88	6.06
Linear regression	2.49	1.79	0.80	4.94	1.02	3.29
SIIE [3]	4.71	3.37	0.99	9.98	1.55	7.50
Quasi U CC [10]	3.94	2.66	0.71	9.16	1.21	5.71
Quasi U CC finetuned [10]	2.55	1.55	0.56	6.15	0.84	3.03
FC4 [32]	2.14	1.64	0.69	4.38	1.15	2.67
FFCC [9]	2.51	2.05	0.80	4.95	1.20	3.20
Ours (200 params)	1.73	1.29	0.37	3.75	0.70	2.32
Ours (470 params)	**0.94**	**0.69**	0.17	**2.14**	0.31	**1.24**
Ours (1460 params)	1.08	0.71	**0.16**	2.57	**0.27**	1.47

Table 3: Angular errors on the main camera from our S20 two-camera dataset. Best results are in bold.

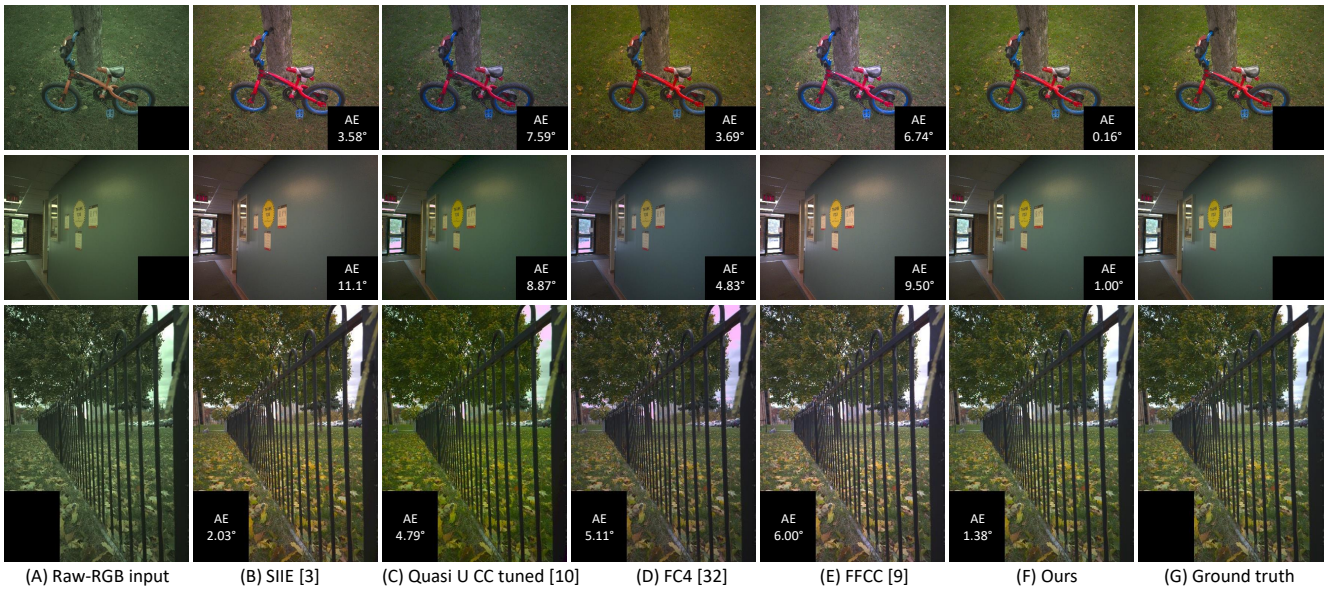

Figure 9: Qualitative results from our real dataset. (A) Input raw-RGB image. (B-F) Results of [3, 10, 32, 9], and our method, respectively, after correcting the input images using the estimated illuminants. (G) Result of correcting using the ground truth illuminant. A gamma has been applied to the raw-RGB images in (A) for illustration. The results in the remaining columns have been rendered to the sRGB color space using [2] to aid visualization. Black boxes are used to mask out the color charts.

in Section 3.1. We then computed the transformation for each image pair. Data augmentation was performed as before to generate a total of 15600 image pairs.

The results on our real dataset are presented in Table 3. Three-fold cross validation was used as before, and training data was augmented for all learning-based methods. As a baseline comparison, we applied a linear regression model in place of our trained network. As seen from Table 3, linear regression yields good results, but our small network performs better because of non-linearities. Results for [3, 32, 9] were computed in the same manner as in Section 4.2. For [10], we fine-tuned the model for each fold using the parameters recommended by the authors. It can be observed that our model with just 200 parameters outperforms all competitors, including FC4 and FFCC. A few qualitative results, along with comparisons, are presented in Fig. 9. Table 4 reports results of training without and with our data augmentation technique. It is evident from the results that our augmentation framework improves performance.

Dataset	**Method**	Mean	Med	B25%	W25%
Real	Ours w/o	2.11	1.46	0.61	4.65
	Ours	**1.73**	**1.29**	**0.37**	**3.75**
NUS	Ours w/o	4.74	2.61	0.66	12.47
	Ours	**2.39**	**1.44**	**0.46**	**5.95**

Table 4: The results of our method with and without (w/o) data augmentation. All models shown have 200 parameters and were trained with a learning rate of 10^{-3}. Best results are in bold.

5. Conclusion

In this work, we take advantage of the availability of two rear-facing cameras, commonly used in modern smartphone design, to perform illumination estimation. Our approach leverages the differences in the sensor's spectral profile between these two cameras. In particular, we trained a lightweight neural network to estimate the scene illumination based on a 3×3 linear color transform that maps between the two cameras' colors. We demonstrated state-of-the-art illuminant estimation performance over contemporary single-image methods through extensive experiments on radiometric data, a quasi-real two-camera dataset generated from an existing single-camera dataset, and a real dataset that we captured using a two-camera smartphone. We believe our work may lead to design changes regarding how current camera devices perform illuminant estimation, leveraging the ubiquity of multi-camera devices. Our code, datasets involving radiometric, quasi-real, and real images from the S20 smartphone, and our trained models will be publicly released to the community. We hope our findings will spur further innovation in smartphone imaging through ideas that leverage multiple cameras.

References

[1] Color constancy : Research website on illuminant estimation. https://colorconstancy.com/source-code/index.html. Accessed: 2020-11-01. 5

[2] Abdelrahman Abdelhamed, Stephen Lin, and Michael S. Brown. A high-quality denoising dataset for smartphone cameras. In *CVPR*, 2018. 8

[3] Mahmoud Afifi and Michael S. Brown. Sensor-independent illumination estimation for DNN models. In *BMVC*, 2019. 2, 6, 7, 8

[4] Mahmoud Afifi, Abhijith Punnappurath, Graham D. Finlayson, and Michael S. Brown. As-projective-as-possible bias correction for illumination estimation algorithms. *JOSA-A*, 36(1):71–78, 2019. 2, 6, 7

[5] Nikola Banic and Sven Loncaric. Color dog - Guiding the global illumination estimation to better accuracy. In *10th International Conference on Computer Vision Theory and Applications*, 2015. 2

[6] Kobus Barnard, Vlad Cardei, and Brian Funt. A comparison of computational color constancy algorithms. I: Methodology and experiments with synthesized data. *TIP*, 11(9):972–984, 2002. 2, 4

[7] Kobus Barnard, Lindsay Martin, Brian Funt, and Adam Coath. A data set for color research. *Color Research & Application*, 27(3):147–151, 2002. 4, 5

[8] Jonathan T. Barron. Convolutional color constancy. In *ICCV*, 2015. 2

[9] Jonathan T. Barron and Yun-Ta Tsai. Fast fourier color constancy. In *CVPR*, 2017. 2, 6, 7, 8

[10] Simone Bianco and Claudio Cusano. Quasi-unsupervised color constancy. In *CVPR*, 2019. 2, 6, 7, 8

[11] Simone Bianco, Claudio Cusano, and Raimondo Schettini. Color constancy using CNNs. In *CVPR Workshops*, 2015. 2

[12] Simone Bianco, Claudio Cusano, and Raimondo Schettini. Single and multiple illuminant estimation using convolutional neural networks. *TIP*, 26(9):4347–4362, 2017. 2

[13] David H. Brainard and William T. Freeman. Bayesian color constancy. *JOSA-A*, 14(7):1393–1411, 1997. 2

[14] David H. Brainard and Brian A. Wandell. Analysis of the retinex theory of color vision. *JOSA-A*, 3(10):1651–1661, 1986. 2, 5, 6, 7

[15] Gershon Buchsbaum. A spatial processor model for object colour perception. *Journal of the Franklin Institute*, 310(1):1 – 26, 1980. 2, 5, 6, 7

[16] Dongliang Cheng, Dilip K. Prasad, and Michael S. Brown. Illuminant estimation for color constancy: Why spatial-domain methods work and the role of the color distribution. *JOSA-A*, 31(5):1049–1058, 2014. 2, 5, 6, 7

[17] Graham Finlayson. Image recording apparatus employing a single CCD chip to record two digital optical images, 2006. US Patent 7,046,288. 2

[18] Graham D. Finlayson. Corrected-moment illuminant estimation. In *ICCV*, 2013. 2, 6, 7

[19] Graham D. Finlayson. Colour and illumination in computer vision. *Interface Focus*, 8, 2018. 2, 6, 7

[20] Graham D. Finlayson, Brian V. Funt, and Kobus Barnard. Color constancy under varying illumination. In *ICCV*, 1995. 5

[21] Graham D. Finlayson, Steven D. Hordley, and Peter Morovic. Chromagenic colour constancy. In *10th Congress of the International Colour Association*, 2005. 2, 3

[22] Graham D. Finlayson, Steven D. Hordley, and Peter Morovic. Colour constancy using the chromagenic constraint. In *CVPR*, 2005. 2, 3

[23] Graham D. Finlayson, Steven D. Hordley, and Ingeborg Tastl. Gamut constrained illuminant estimation. *IJCV*, 67(1):93–109, 2006. 2

[24] Graham D. Finlayson and Elisabetta Trezzi. Shades of gray and colour constancy. In *Color Imaging Conference*, 2004. 2, 5, 6, 7

[25] David A. Forsyth. A novel algorithm for color constancy. *IJCV*, 5:5–35, 2004. 2

[26] Peter V. Gehler, Carsten Rother, Andrew Blake, Tom Minka, and Toby Sharp. Bayesian color constancy revisited. In *CVPR*, 2008. 2

[27] Arjan Gijsenij and Theo Gevers. Color constancy using natural image statistics and scene semantics. *TPAMI*, 33(4):687–698, 2011. 2

[28] Arjan Gijsenij, Theo Gevers, and Joost Van De Weijer. Generalized gamut mapping using image derivative structures for color constancy. *IJCV*, 86:127–139, 2008. 2, 5, 6, 7

[29] Arjan Gijsenij, Theo Gevers, and Joost Van De Weijer. Improving color constancy by photometric edge weighting. *TPAMI*, 34(5):918–929, 2012. 5, 6, 7

[30] Google. Android Camera2 API. https://developer.android.com/reference/android/hardware/camera2/package-summary.html. Accessed: 2017-11-10. 7

[31] Daniel Hernandez-Juarez, Sarah Parisot, Benjamin Busam, Ales Leonardis, Gregory Slabaugh, and Steven McDonagh. A multi-hypothesis approach to color constancy. In *CVPR*, 2020. 2

[32] Yuanming Hu, Baoyuan Wang, and Stephen S Lin. FC4: Fully convolutional color constancy with confidence-weighted pooling. In *CVPR*, 2017. 2, 6, 7, 8

[33] Jun Jiang, Dengyu Liu, Jinwei Gu, and Sabine Süsstrunk. What is the space of spectral sensitivity functions for digital color cameras? In *WACV*, 2013. 4, 5

[34] Hamid Reza Vaezi Joze and Mark S. Drew. Exemplar-based color constancy and multiple illumination. *TPAMI*, 36(5):860–873, 2014. 2

[35] Hamid Reza Vaezi Joze, Mark S. Drew, Graham D. Finlayson, and Perla Aurora Troncoso Rey. The role of bright pixels in illumination estimation. In *Color Imaging Conference*, 2012. 2

[36] Hakki C. Karaimer and Michael S. Brown. A software platform for manipulating the camera imaging pipeline. In *ECCV*, 2016. 2

[37] Diederik P. Kingma and Jimmy Ba. Adam: A method for stochastic optimization. *ICLR*, 2014. 5

[38] Zhongyu Lou, Theo Gevers, Ninghang Hu, and Marcel P. Lucassen. Color constancy by deep learning. In *BMVC*, 2015. 2

[39] Laurence T. Maloney. Physics-based approaches to modeling surface color perception. *Color vision: From genes to perception*, 1999. 1

[40] Simon Niklaus, Xuaner Cecilia Zhang, Jonathan T. Barron, Neal Wadhwa, Rahul Garg, Feng Liu, and Tianfan Xue. Learned dual-view reflection removal. *arXiv preprint arXiv:2010.00702*, 2020. 1

[41] Seoung Oh and Seon Kim. Approaching the computational color constancy as a classification problem through deep learning. *Pattern Recognition*, 2016. 2

[42] Dilip K. Prasad. Strategies for resolving camera metamers using 3+1 channel. In *CVPR Workshop*, 2016. 2

[43] Yanlin Qian, Ke Chen, Jarno Nikkanen, Joni-Kristian Kamarainen, and Jiri Matas. Recurrent color constancy. In *ICCV*, 2017. 2

[44] Charles Rosenberg, Alok Ladsariya, and Tom Minka. Bayesian color constancy with non-gaussian models. In *NeurIPS*. 2004. 2

[45] Wu Shi, Chen Change Loy, and Xiaoou Tang. Deep specialized network for illuminant estimation. In *ECCV*, 2016. 2

[46] Joost Van De Weijer, Theo Gevers, and Arjan Gijsenij. Edge-based color constancy. *TIP*, 16(9), 2007. 2, 5, 6, 7

[47] Jin Xiao, Shuhang Gu, and Lei Zhang. Multi-domain learning for accurate and few-shot color constancy. In *CVPR*, 2020. 2

[48] Yinda Zhang, Neal Wadhwa, Sergio Orts-Escolano, Christian Häne, Sean Fanello, and Rahul Garg. Du2net: Learning depth estimation from dual-cameras and dual-pixels. *arXiv preprint arXiv:2003.14299*, 2020. 1

IIRC: Incremental Implicitly-Refined Classification

Mohamed Abdelsalam[1,2], Mojtaba Faramarzi[1,2], Shagun Sodhani[3], Sarath Chandar[1,4,5]

[1]Mila - Quebec AI Institute, [2]University of Montreal, [3]Facebook AI Research,
[4]École Polytechnique de Montréal, [5]Canada CIFAR AI Chair
{abdelsam, faramarm, sarath.chandar}@mila.quebec, sshagunsodhani@gmail.com

Abstract

We introduce the "Incremental Implicitly-Refined Classification (IIRC)" setup, an extension to the class incremental learning setup where the incoming batches of classes have two granularity levels. i.e., each sample could have a high-level (coarse) label like "bear" and a low-level (fine) label like "polar bear". Only one label is provided at a time, and the model has to figure out the other label if it has already learned it. This setup is more aligned with real-life scenarios, where a learner usually interacts with the same family of entities multiple times, discovers more granularity about them, while still trying not to forget previous knowledge. Moreover, this setup enables evaluating models for some important lifelong learning challenges that cannot be easily addressed under the existing setups. These challenges can be motivated by the example "if a model was trained on the class bear in one task and on polar bear in another task, will it forget the concept of bear, will it rightfully infer that a polar bear is still a bear? and will it wrongfully associate the label of polar bear to other breeds of bear?". We develop a standardized benchmark that enables evaluating models on the IIRC setup. We evaluate several state-of-the-art lifelong learning algorithms and highlight their strengths and limitations. For example, distillation-based methods perform relatively well but are prone to incorrectly predicting too many labels per image. We hope that the proposed setup, along with the benchmark, would provide a meaningful problem setting to the practitioners.

1. Introduction

Deep learning algorithms have led to transformational breakthroughs in computer vision [12, 17], natural language processing [19, 50], speech processing [3, 5], reinforcement learning [36, 44], robotics [16, 1], recommender systems [11, 18], etc. On several tasks, deep learning models have either matched or surpassed human performance. However, such *super-human* performance is limited to some narrow and well-defined setups. Moreover, humans can continually learn and accumulate knowledge over their lifetime, while the current learning algorithms are known to suffer from several challenges when training over a sequence of tasks [33, 15, 8, 45]. These challenges are broadly studied under the domain of Lifelong Learning [47], also called Incremental Learning [42], Continual Learning [48], and Never Ending Learning [35]. In the general lifelong learning setup, the model experiences new knowledge, in terms of new tasks, from the same or different domains. The model is expected to learn and solve new tasks while retaining useful knowledge from previous tasks.

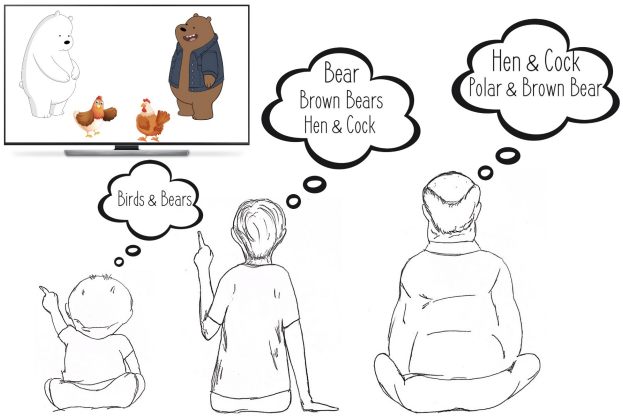

Figure 1. Humans incrementally accumulate knowledge over time. They encounter new entities and discover new information about existing entities. In this process, they associate new *labels* with entities and refine or update their existing *labels*, while ensuring the accumulated knowledge is coherent.

There are two popular paradigms in lifelong learning [49]: **i)** *task incremental* learning, where the model has access to a task delimiter (say a *task id*), which distinguish between tasks. Models for this setup are generally multi-headed, where there exists a separate classification layer for each task. **ii)** *class incremental learning*, where the model does not have access to a task delimiter, so it needs to discriminate between all classes from all tasks at infer-

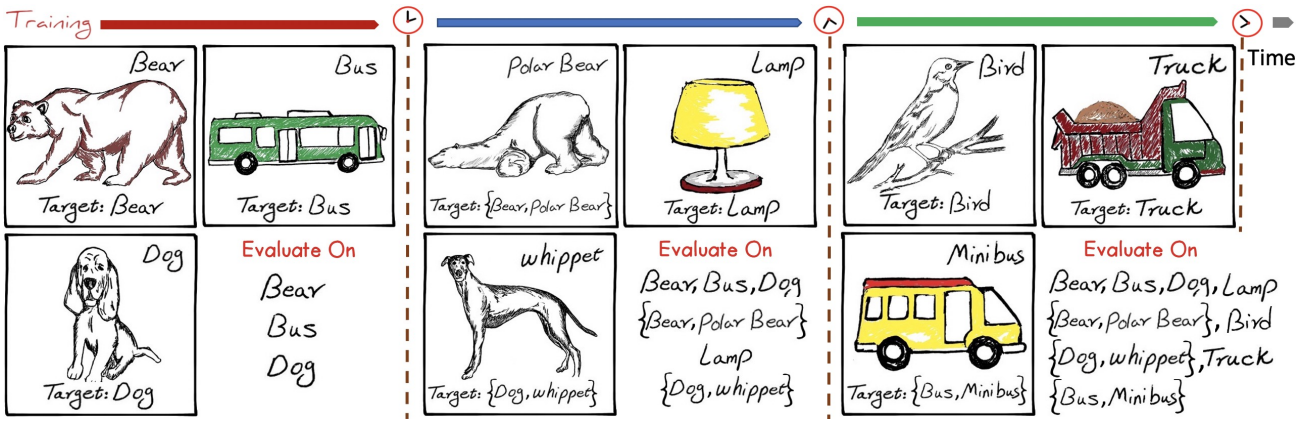

Figure 2. IIRC setup showing how the model expands its knowledge and associates and re-associates labels over time. The top right label shows the label model sees during training, and the bottom label (annotated as "Target") is the one that model should predict during evaluation. The right bottom panel for each task shows the set classes that model is evaluated on and the dashed line shows different tasks.

ence time. Therefore, models developed for this paradigm are generally single-headed. The class incremental setup is more closely aligned with the real-life scenarios and is more challenging than the task incremental scenario.

Several useful benchmarks have been proposed for evaluating models in the lifelong learning setting [4, 25]. While useful for measuring high-level aggregate quantities, these benchmarks take a narrow and limited view on the broad problem of lifelong learning. One common assumption that many class incremental setups make is "information about a given sample (say label) can not change across tasks". For example, an image of a bear is always labeled as "bear", no matter how much knowledge the model has acquired.

While this assumption appears to be "obviously correct" in the context of the supervised learning paradigm (where each sample generally has a fixed label), the assumption is not always satisfied in real-life scenarios. We often interact with the same entities multiple times and discover new information about them. Instead of invalidating the previous knowledge or outright rejecting the new information, we refine our previous knowledge using the new information. Figure 1 illustrates an example where a child may recognize all bears as "bear" (and hence label them as "bear"). However, while growing up, they may hear different kinds of bear being called by different names, and so they update their knowledge as: "Some bears are brown bears, some bears are polar bears, and other bears are just bears. Brown bears and polar bears are both still bears but they are distinct". This does not mean that their previous knowledge was wrong (or that previous label "bear" was "incorrect"), but they have discovered new information about an entity and have coherently updated their knowledge. This is the general scheme of learning in humans.

A concrete instantiation of this learning problem is that two similar or even identical input samples have two different labels across two different tasks. We would want the model to learn the new label, associate it with the old label without forgetting the old label. Evaluating lifelong learning models for these capabilities is generally outside the scope of existing benchmarks. We propose the *Incremental Implicitly-Refined Classification (IIRC)* setup to fill this gap. We adapt the publicly available CIFAR100 and ImageNet datasets to create a benchmark for the IIRC setup and evaluate several well-known algorithms on this benchmark. Our goal is not to develop a new state-of-the-art model but to surface the challenges posed by the IIRC setup.

The main contributions of our work are as follows:

1. We propose the *Incremental Implicitly-Refined Classification (IIRC)* setup, where the model starts training with some coarse, high-level classes and observes new, fine-grained classes as it trains over new tasks. During the lifetime of the model, it may encounter a new sample or an old sample with a fine-grained label.

2. We provide a standardized benchmark to evaluate a lifelong model in the IIRC setup. We adapt the commonly used ImageNet and CIFAR datasets, and provide a benchmark setup compatible with several major deep learning frameworks (PyTorch and Tensorflow)[1].

3. We evaluate well-known lifelong learning algorithms on the benchmark and highlight their strengths and limitations, while ensuring that the models are compared in a fair and standardized setup.

2. Incremental Implicitly-Refined Classification (IIRC)

While class incremental learning is a challenging and close-to-real-life formulation of the lifelong learning setup, most existing benchmarks do not explore the full breadth

[1] https://chandar-lab.github.io/IIRC/

of the complexity. They tend to over-focus on catastrophic forgetting (which is indeed an essential aspect) at the expense of several other unique challenges to the class incremental learning. In this work, we highlight those challenges and propose the *Incremental Implicitly-Refined Classification (IIRC)* setting, an extension of the class incremental learning setting, that enables us to study these under-explored challenges, along with the other well-known challenges like catastrophic forgetting. We provide an instantiation of the setup, in the form of a benchmark, and evaluate several well-known lifelong learning algorithms on it.

2.1. Under-explored challenges in class incremental learning setting

In class incremental learning, the model encounters new classes as it trains over new tasks. The nature of the class distributions and the relationship between classes (across tasks) can lead to several interesting challenges for the learning model: If the model is trained on a *high-level* label (say "bear") in the initial task and then trained on a *low-level* label, which is a refined category of the previous label (say "polar bear"), what kind of associations will the model learn and what associations will it forget? Will the model generalize and label the images of polar bear as both "bear" and "polar bear"? Will the model catastrophically forget the concept of "bear"? Will the model infer the spurious correlation: "all bears are polar bears"? What happens if the model sees different labels (at different levels of granularity) for the *same sample* (across different tasks)? Does the model remember the latest label or the oldest label or does it remember all the labels? These challenges can not be trivially overcome by removing restrictions on memory or replay buffer capacity (as we show in Section 6).

2.2. Terminology

We describe the terminology used in the paper with the help of an example. As shown in Figure 2, at the start, the model trains on data corresponding to classes "bear", "bus" and "dog". Training the model on data corresponding to these three classes is the first **task**. After some time, a new set of classes ("polar bear", "lamp" and "whippet") is encountered, forming the second task. Since "whippet" is a type of "dog", it is referred to as a **subclass**, while "dog" is referred to as a **superclass**. The "dog-whippet" pair is referred to as the superclass-subclass pair. Some classes do not have a superclass (example "lamp"), we refer to these classes as subclasses as well. When training the model on an example of a "whippet", we may provide only "whippet" as the supervised learning label. This setup is referred to as the **incomplete information** setup, where if a task sample has two labels, only the label that belongs to the current task is provided. Alternatively, we may provide both "whippet" and "dog" as the supervised learning labels. This setup is referred as the **complete information** setup, where if a task sample has two labels, labels that belong to the current or previous tasks are provided. The majority of our experiments are performed in the incomplete information setup as it is closer to the real life setup, requiring the model to recall the previous knowledge when it encounters some new information about a known entity. We want to emphasize that the use of the word **task** in our setup refers to the arrival of a new batch of classes for the model to train on in a single-head setting, and so it is different from it's use to indicate a distinct classification head in task incremental learning.

As the model is usually trained in an *incomplete information* setup, it needs access to a validation set to monitor the progress in training that is also an *incomplete information* set, otherwise there would be some sort of labels leakage. On the other hand, after training on a specific task, the model has to be evaluated on a *complete information* set, hence a *complete information* validation set is needed to be used during the process of model development and tweaking, so as to not overfit on the test set. We provide both in the benchmark. We call the first one the **in-task validation set**, while the latter one the **post-task validation set**.

2.3. Setup

We describe the high-level design of the IIRC setup (for a visual illustration, see Figure 2). We have access to a series of N tasks denoted as $T_1, \cdots, T_N$. Each task comprises of three collections of datasets, for training, validation and testing. Each sample can have one or two labels associated with it. In the case of two labels, one label is a subclass and the other label is a superclass. For any superclass-subclass pair, the superclass is always introduced in an earlier task, with the intuition that a high-level label should be relatively easier to learn. Moreover, the number of samples for a superclass is always more than the number of samples for a subclass (it increases with the number of subclasses, up to a limit). During training, we always follow the incomplete information setup. During the first task, only a subset of superclasses (and no sublcasses) are used to train the model. The first task has more classes (and samples), as compared to the other tasks and it can be seen as a kind of pretraining task. The subsequent tasks have a mix of superclasses and subclasses. During the training phase, the model is evaluated on the in-task validation set (with incomplete information), and during the evaluation phase, the model is evaluated on the post-task validation set and the test set (both with complete information).

3. Related Work

Lifelong Learning is a broad, multi-disciplinary, and expansive research domain with several synonyms: Incremental Learning [42], Continual Learning [48], and Never Ending Learning [35]. One dimension for organizing the ex-

isting literature is whether the model has access to explicit task delimiters or not, where the former case is referred to as task incremental learning, and the latter case, which is closely related to our setup IIRC, is referred to as class incremental learning.

In terms of learning methods, there are three main approaches [23]: **i)** replay based, **ii)** regularization based, and **iii)** parameter isolation methods. Parameter isolation methods tend to be computationally expensive and require access to a task identifier, making them a good fit for the task incremental setup. Prominent works that follow this approach include Piggyback [29], PackNet [30], HAT [43], TFM [32], DAN [40], PathNet [14]. The replay and regularization based approaches can be used with both task and class incremental setups, however, replay based approaches usually perform better in the class incremental setup [31]. Among the regularization based approaches, LwF [24] uses finetuning with distillation. LwM [13] improves LwF by adding an attention loss. MAS [2], EWC [21], SI [52] and RWalk [8] estimate the importance of network parameters, and penalize changes to important ones. As for the replay based approaches, iCaRL [38] is considered an important baseline in the field. iCaRL selects exemplars for the replay buffer using herding strategy, and alleviates catastrophic forgetting by using distillation loss during training, and using a nearest-mean-of-exemplars classifier during inference. EEIL [7] modifies iCaRL by learning the feature extractor and the classifier jointly in an end to end manner. LUCIR [20] applies the distillation loss on the normalized latent space rather than the output space, proposes to replace the standard softmax layer with a cosine normalization layer, and uses a margin ranking loss to ensure a large margin between the old and new classes. Other works include LGM [37], IL2M [6], BIC [51], and ER [39]. GEM is another replay-based method, which solves a constrained optimization problem. It uses the replay buffer to constrain the gradients on the current task so that the loss on the previous tasks does not increase. A-GEM [9] improves over GEM by relaxing some of the constraints, and hence increasing the efficiency, while retaining the performance. Finally, [10] shows that vanilla experience replay, where the model simply trains on the replay buffer along with the new task data, is by itself a very strong baseline. In this work, we include variants of iCaRL, LUCIR, A-Gem, and vanilla experience replay as baselines.

We propose a benchmark for evaluating a model's performance in the IIRC setup, as having a realistic, standardized, and large-scale benchmark helps provide a fair and reproducible comparison for the different approaches. Existing efforts for benchmarking the existing lifelong learning setups include CORe50 benchmark [25], and [4] that proposes a benchmark for continual few-shot learning.

Our work is also related to knowledge (or concept) drift, where the statistical properties of the data changes over time and old knowledge can become "irrelevant" [28, 27]. Unlike those works, we focus on learning new associations and updating existing associations as new tasks are learnt. As the model acquires new knowledge, the old knowledge does not become 'irrelevant". Recently, BREEDS [41] proposed a benchmark to evaluate model's generalization capabilities in the context of subpopulation shift. Specifically, they define a hierarchy and train the model on samples corresponding to some subpopulations (e.g. "poodles" and "terriers" are subpopulations of "dogs"). The model is then evaluated on samples from an unseen subpopulation. e.g. it should label "dalmatians" as "dogs". While at a quick glance, IIRC might appear similar to BREEDS, there are several differences. IIRC focuses on the lifelong learning paradigm while BREEDS focuses on generalization. Moreover, the training and evaluation setups are also different. If we were to extend the dogs example to IIRC, the model may first train on some examples of "poodles" and "terriers" (labeled as "dogs"). In the next task, it may train on some exampled of "poodles" (labeled as "poodles"). When the model is evaluated on both tasks, it should predict both labels ("poodles" and "dogs") for the images of poodles.

4. Benchmark

4.1. Dataset

We use two popular computer vision datasets in our benchmark - ImageNet [12] and CIFAR100 [22]. For both the datasets, we create a two-level hierarchy of class labels, where each label starts as a leaf-node and similar labels are assigned a common parent. The leaf-nodes are the *sub-classes* and the parent-nodes are the *super-classes*. Some of the subclasses do not have a corresponding superclass, so as to enrich the setup and make it more realistic. While the datasets come with a pre-defined hierarchy (e.g. ImageNet follow the WordNet hierarchy), we develop a new hierarchy as the existing hierarchy focuses more on the semantics of the labels and less on the visual similarity (e.g, in WordNet, "sliding door" and "fence" are both grouped under "barriers"). We refer to these adapted datasets as IIRC-ImageNet and IIRC-CIFAR.

In IIRC-CIFAR, each superclass has similar number of subclasses (four to eight). However, the sub-class distribution for IIRC-ImageNet is very skewed (Figure A.7) and number of sublcasses varies from 3 to 118. We explicitly decided not to *fix* this imbalance to ensure that visually similar classes are grouped together. Moreover, in the real life, not all classes are observed at the same frequency, making our setup more realistic. More statistics and the full class hierarchies for both IIRC-ImageNet and IIRC-CIFAR are provided in Appendix-C and G.

As mentioned in Section 2, we use two validation sets -

one with incomplete information (for model selection and monitoring per-task performance) and one with complete information (for the model evaluation after each task). Each validation dataset comprises 10% of the training data for CIFAR, and 4% of the training data for ImageNet, and is fixed through all the runs. Some aggregate information about the splits is provided in Table 1 in Appendix.

Since we are creating the class hierarchy, superclasses do not have any samples assigned to them. For the training set and the in-task validation set, we assign 40% of samples from each subclass to its superclass, while retaining 80% of the samples for the subclass. This means that subclass-superclass pairs share about 20% of the samples or, for 20% of the cases, the model observes the same sample with different labels (across different tasks). Since some superclasses have an extremely large number of subclasses, we limit the total number of samples in a superclass. A superclass with more than eight subclasses, uses $\frac{8}{\text{number of subclasses}} \times 40\%$ of samples from its subclasses. We provide the pseudo code for the dataloader in Appendix F.

Now that we have a dataset with superclasses and subclasses, and with samples for both kind of classes, the tasks are created as follows: The first task is always the largest task with 63 superclasses for IIRC-ImageNet and 10 superclasses for IIRC-CIFAR. In the supsequent tasks, each new task introduces 30 classes for IIRC-ImageNet and 5 classes for IIRC-CIFAR. Recall that each task introduces a mix of superclasses and subclasses. IIRC-ImageNet has a total of 35 tasks, while IIRC-CIFAR has a total of 21 tasks. Since the order of classes can have a bearing on the models' evaluation, we create 5 preset class orders (called task configurations) for IIRC-ImageNet and 10 task configurations for IIRC-CIFAR, and report the average (and standard deviation) of the performance on these configurations.

Finally, we acknowledge that while IIRC-ImageNet provides interesting challenges in terms of data diversity, training on the dataset could be difficult and time consuming. Hence, we provide a shorter, lighter version which has just ten tasks (with five tasks configurations). We shall call the original version IIRC-ImageNet-full, and the lighter version IIRC-ImageNet-lite, while referring to both collectively as IIRC-ImageNet. Although we do not recommend the use of this lighter version for benchmarking the model performance, we hope that it will make it easier for others to perform quick, debugging experiments. We report all the metrics on IIRC-ImageNet-lite as well.

4.2. Metrics

Most lifelong learning benchmarks operate in the single-label classification setup, making accuracy the appropriate metric. In our setup, the model should be able to predict multiple labels for each sample, even if those labels are seen across different tasks. We considered using the *Exact-Match Ratio* (MR) metric [46], a multi-label extension of the accuracy metric. MR is defined as $\frac{1}{n}\sum_{i=1}^{n} I(Y_i == \hat{Y}_i)$ where I is the indicator function, $\hat{Y}_i$ are the set of (model) predictions for the i_{th} sample, Y_i are the ground truth labels, and n is the total number of samples. One limitation is that it does not differentiate between partially incorrect predictions and completely incorrect predictions.

Another popular metric (for multi-label classification) is the Jaccard similarity(JS), also called "intersection over union"[46]. JS is defined as $\frac{1}{n}\sum_{i=1}^{n} \frac{|Y_i \cap \hat{Y}_i|}{|Y_i \cup \hat{Y}_i|}$. To further penalize the imprecise models, we *weight* the Jaccard similarity by the per sample precision (i.e., the ratio of true positives over the sum of true positives and false positives). We refer to this metric as the *precision-weighted Jaccard similarity (pw-JS)*.

We measure the performance of a model on task k after training on task j using the precision-weighted Jaccard similarity, denoted R_{jk}, as follow:

$$R_{jk} = \frac{1}{n_k}\sum_{i=1}^{n_k} \frac{|Y_{ki} \cap \hat{Y}_{ki}|}{|Y_{ki} \cup \hat{Y}_{ki}|} \times \frac{|Y_{ki} \cap \hat{Y}_{ki}|}{|\hat{Y}_{ki}|}, \qquad (1)$$

where ($j \geq k$), $\hat{Y}_{ki}$ is the set of (model) predictions for the i_{th} sample in the k_{th} task, Y_{ki} are the ground truth labels, and n_k is number of samples in the task. R_{jk} can be used as a proxy for the model's performance on the k^{th} task as it trains on more tasks (i.e. as the j increases).

We evaluate the overall performance of the model after training till the task j, as the average *precision-weighted Jaccard similarity* over all the classes that the model has encountered so far. Note that during this evaluation, the model has to predict all the correct labels for a given sample, even if the labels were seen across different tasks (i.e. the evaluation is performed in the complete information setup). We denote this metric as R_j and computed it as follow:

$$R_j = \frac{1}{n}\sum_{i=1}^{n} \frac{|Y_i \cap \hat{Y}_i|}{|Y_i \cup \hat{Y}_i|} \times \frac{|Y_i \cap \hat{Y}_i|}{|\hat{Y}_i|}, \qquad (2)$$

where n is the total number of evaluation samples for all the tasks seen so far.

5. Baselines

We evaluate several well-known lifelong learning baselines. We also consider two training setups where the model has access to all the labels for a given sample (complete information setup): **i)** *joint* where the model is jointly trained on all the classes/tasks at once and **ii)** *incremental joint* where as the model trains across tasks, it has access to all the data from the previous tasks in a *complete information* setup. In the **Finetune** baseline, the model continues training on new batches of classes without using any replay

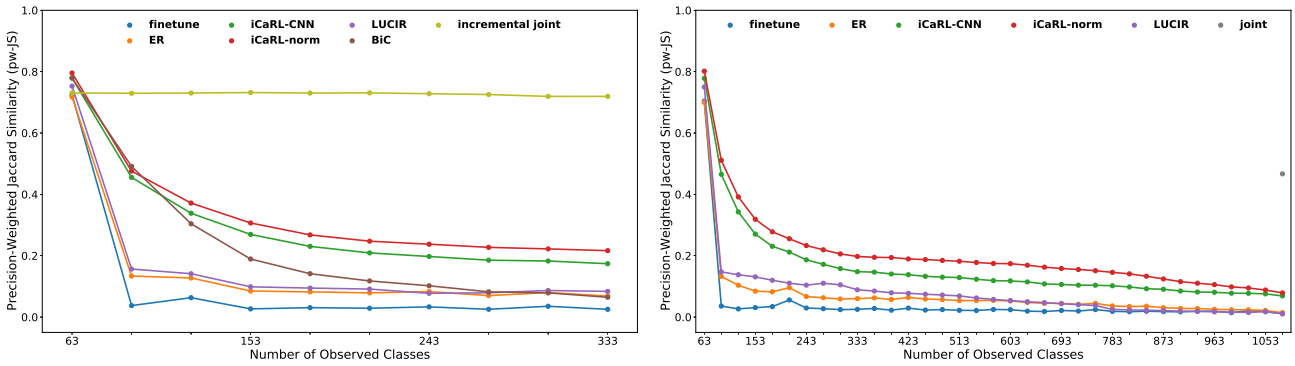

Figure 3. Average performance using the precision-weighted Jaccard Similarity. (left) IIRC-ImageNet-lite and (right) IIRC-ImageNet-full. Experiments are averaged over five different task configurations with the mean reported. (see Figure A.8 for the standard deviation)

buffer. Vanilla **Experience Replay (ER)** method finetunes the model on new classes, while keeping some older samples in the replay buffer and rehearsing on them. **Experience Replay with infinite buffer (ER-infinite)** is similar to *incremental joint*, but in *incomplete information* setup as in ER. This means that if a new label is introduced that applies to an old sample, the target for that sample will be updated with that new label in the incremental joint baseline but not in the ER-infinte baseline . We also have **A-GEM** [9] that is a constrained optimization method in the replay-based methods category. It provides an efficient version of GEM [26] by minimizing the average memory loss over the previous tasks at every training step. Another baseline is **iCaRL** [38] that proposed using the exemplar rehearsal along with a distillation loss. **LUCIR** [20] is a replay-based class incremental method that alleviates the catastrophic forgetting and the negative effect of the imbalance between the older and newer classes. **BiC** [51] adds a bias correction step after each task to counteract the bias towards newer classes. More details about the baselines can be found in Appendix-B.

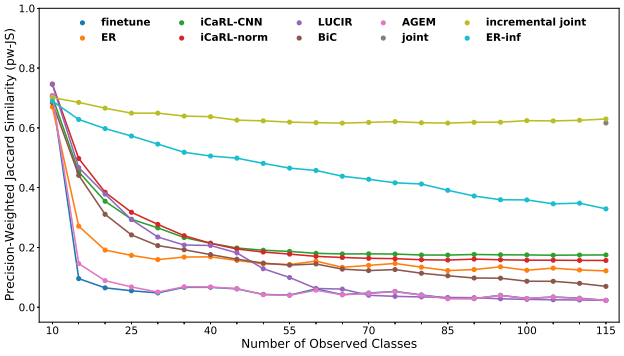

Figure 4. Average performance on IIRC-CIFAR. Experiments are averaged over ten different task configurations with the mean reported. (see Figure A.8 for the standard deviation)

5.1. Model Adaptations

The earlier-stated baselines were proposed for the single label class incremental setup, while IIRC setup requires the model to be able to make multi-label predictions. Therefore, some changes have to be applied to the different models to make them applicable in the IIRC setup. To this end, we use the binary cross-entropy loss (BCE) as the classification loss. This loss is averaged by the number of observed classes so that it doesn't increase as the number of classes increases during training. During prediction, a sigmoid activation is used and classes with values above 0.5 are considered the predicted labels. Using the nearest-mean-classifier strategy for classifying samples in iCaRL is not feasible for our setting, as the model should be able to predict a variable number of labels. To overcome this issue, we use the output of the classification layer, which was used during training, and call this variant as iCaRL-CNN. We further consider a variant of iCaRL-CNN, called iCaRL-norm, which uses cosine normalization in the last layer. [20] suggests that using this normalization improves the performance in the context of incremental learning. Hence the classification score is calculated as:

$$p_i(x) = \sigma(\eta \langle \bar{\theta}_i \, , \bar{f}(x) \rangle) \, , \tag{3}$$

where σ is the sigmoid function, $\bar{\theta}_i$ are the normalized weights of the last layer that correspond to label i, and $\bar{f}(x)$ is the output of the last hidden layer for sample x. η is a learnable scalar that controls the peakiness of the sigmoid. It is important to have η since $\langle \bar{\theta}_i \, , \bar{f}(x) \rangle$ is restricted to $[-1, 1]$. We can either fix the η or consider it as a learnable parameter. We observed that learning η works better in practice.

6. Experiments

We design our experimental setup to surface challenges that lifelong learning algorithms face when operating in the

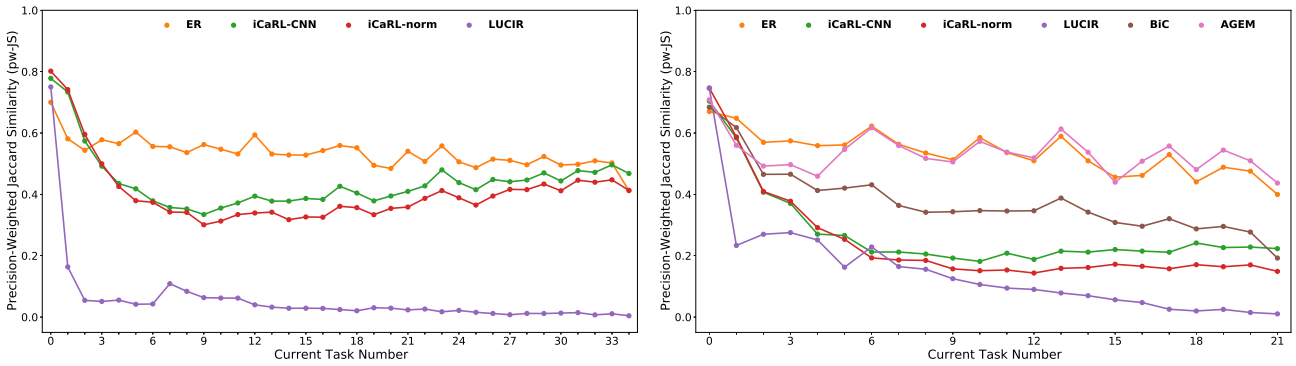

Figure 5. Per task performance over the test samples of a specific task j, after training on that task (R_{jj} using Equation 1). (left) IIRC-ImageNet-full and (right) IIRC-CIFAR. see Figure A.9 for the standard deviation)

IIRC setup. Our goal is neither to develop a new state-of-the-art model nor to rank existing models. We aim to highlight the strengths and weakness of the dominant lifelong learning algorithms, with the hope that this analysis will spur new research directions in the field. We use the ResNet architecture [17], with ResNet-50 for IIRC-ImageNet and reduced ResNet-32 for IIRC-CIFAR. Additional implementation details and hyperparameters can be found in Section A in the Appendix. Data used to plot the figures is provided in Appendix H for easier future comparisons.

6.1. Results and Discussion

We start by analyzing how well does the model perform over all the observed classes as it encounters new classes. Specifically, as the model finishes training on the j^{th} task, we report the average performance R_j, as measured by the *pw-JS* metric using Equation 2, over the evaluation set of all the tasks the model has seen so far (Figures 3 and 4). Recall that when computing R_j, the model has to predict all the correct labels for a given sample, even if the labels were seen across different tasks. This makes R_j a challenging metric as the model can not achieve a good performance just by memorizing the older labels, but it has to learn the relationship between labels.

In Figures 3 and 4, we observe that the iCaRL-CNN and iCaRL-norm models perform relatively better than the other methods, with iCaRL-norm having the edge in the case of IIRC-ImageNet. However, this trend does not describe the full picture, as the iCaRL family of models is usually predicting more labels (some of which are incorrect). This behaviour can be observed for the IIRC-CIFAR setup in Figure 6(c) where they tend to predict too many labels incorrectly, which penalize their performance with respect to the PW-JS metric as opposed to the JS metric (see Figure A.15 in the Appendix). We also note that A-GEM model performs poorly in the case of IIRC-CIFAR, even when compared to vanilla ER, and hence we didn't run A-GEM on IIRC-ImageNet.

One thing to notice in Figure 4, is the discrepancy between the performance of the ER-infinite baseline and the incremental joint baseline. Recall from section 5 that although both baselines don't discard previous tasks samples, incremental joint is using the *complete information* setup, and hence it updates the older samples with the newly learned labels if applicable, while ER-infinite is using the *incomplete information* setup. This result tells us that dealing with the memory constraint is not sufficient by itself for a model to be able to perform well in the IIRC setup.

In lifelong learning setups, the model should retain the previous knowledge as it learns new tasks. Our setup is even more challenging because the model should not only retain previous knowledge, but it should incorporate the new labels as well in this previous knowledge. In Figure A.16 and A.17, we track how well the model performs on a specific task, as it is trained on subsequent tasks. Unlike the standard class incremental setup, the model should be able to re-associate labels across different tasks to keep performing well on a previous task. The key takeaway is that, while the baselines are generally expected to reasonably alleviate catastrophic forgetting, their performance degrades rapidly as the model trains on more tasks. ER's poor performance may be accounted for by two hypothesis: **i)** The model is trained on a higher fraction of samples per class for classes that belong to the current task, than those of previous tasks, causing bias towards newer classes. **ii)** The model sometimes gets conflicting supervising signal, as the model might observe samples that belong to the same subclass (ex. "polar bear"), once with the superclass label from the buffer ("bear"), and another with the subclass label from the current task data ("polar bear'), and it doesn't connect these two pieces of information together. In the case of LUCIR, we hypothesize that the model's performance deteriorates because the model fails to learn new class labels. We confirm this hypothesis in Figure 5 and Figure A.22, where we

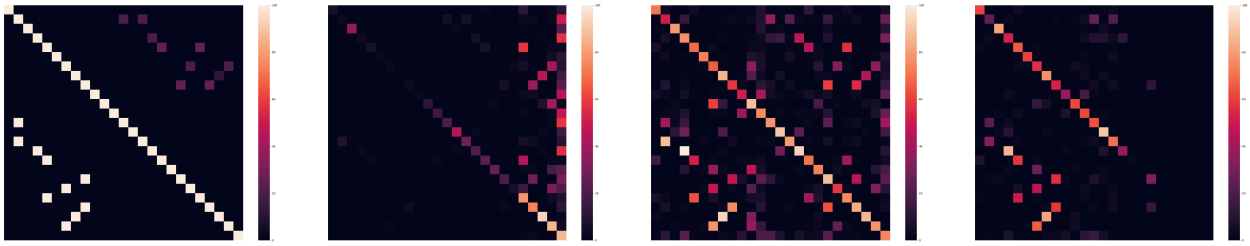

(a) ground truth (b) ER (c) iCaRL-norm (d) LUCIR

Figure 6. Confusion matrix after training on task 10 of IIRC-CIFAR. The y-axis is the correct label (or one of the correct labels). The x-axis is the model predicted labels. Labels are arranged by their order of introduction. Only 25 labels are shown for better visibility. See Appendix D.7 for the full resolution figures with labels.

observe that while the model is able to retain the labels encountered in the previous tasks, it is not able to learn the labels it encounters during the new tasks. We can see as well in Figure 5 the performance of each model on the current task j, after training on that task (R_{jj} using Equation 1). The general trend is that the less a model is regularized, the higher it can perform on the current task, which is intuitive.

Some other important questions are whether the model correctly associates the newly learned subclass labels to their previously learned superclass, and whether it incorrectly associates the newly learned subclass label with other previously learned subclasses (that have the same superclass). We dig deeper into the confusion matrix (Figure 6) for the predictions of the different models after training on ten tasks of IIRC-CIFAR. Note that in Figure 6, the lower triangular matrix shows the percentage the model predicts older labels for the newly introduced classes, while the upper triangular matrix represents the percentage the model predict newer labels to older classes, with the ground truth being Figure 6(a). The ER method predictions always lie within the newly learned labels (last five classes), as shown in Figure 6(b)) The iCaRL-norm model, as shown in Figure 6(c), performs relatively well in terms of associating (previosuly learned) superclasses to (newly learned) subclasses. For example, whales are always correctly labeled as aquatic mammals, and pickup trucks are correctly labeled as vehicles 94% of the time. However, these models learn some spurious associations as well. For instance, "television" is often mislabeled as "food containers". Similarly, the model in general correctly associates newer subclasses with older superclasses, but many times it incorrectly associates the subclasses (eg associating " aquatic mammals" with "whales" 48% of the time and "vehicles" with "pickup trucks" 44% of the time, while by looking at figure 6(a), we see that they only represent 20% and 12.5% of their superclasses respectively) The LUCIR model provides accurate superclass labels to the subclasses. This is shown in Figure 6(d) where LUCIR follows the trends of the ground truth more closely than iCaRL-norm in the lower triangular part of the confusion matrix. However, it fails to learn new associations. We provide more instances of such plots in the Appendix D.6, which shows that the observed trends are quite general. The full resolution figures for Figure 6 are provided in Appendix D.7. We also provide some more finegrained plots for the performance on each of the class types in the Appendix D.2 and D.3.

Finally, we provide some ablations for the effect of the buffer size using ER in Appendix E. We can see that using ER even with a buffer size of 100 samples per class gives very poor performance in the case of IIRC-ImageNet, and hence a smarter strategy is needed for this setup.

7. Conclusion

We introduced the "Incremental Implicitly-Refined Classification (IIRC)" setup, a novel extension for the class incremental learning setup where incoming batches of classes have labels at different granularity. Our setup enables studying different challenges in the lifelong learning setup that are difficult to study in the existing setups. Moreover, we proposed a standardized benchmark for evaluating the different models on the IIRC setup. We analyze the performance of several well-known lifelong learning models to give a frame of reference for future works and to bring out the strengths and limitations of different approaches. We hope this work will provide a useful benchmark for the community to focus on some important but under-studied problems in lifelong learning.

Acknowledgments

We would like to thank Louis Clouatre and Sanket Vaibhav Mehta for reviewing the paper and for their meaningful feedback. We would like also to thank Louis for suggesting the task name. SC is supported by a Canada CIFAR AI Chair and an NSERC Discovery Grant.

References

[1] Ilge Akkaya, Marcin Andrychowicz, Maciek Chociej, Mateusz Litwin, Bob McGrew, Arthur Petron, Alex Paino, Matthias Plappert, Glenn Powell, Raphael Ribas, et al. Solving rubik's cube with a robot hand. *arXiv preprint arXiv:1910.07113*, 2019.

[2] Rahaf Aljundi, Francesca Babiloni, Mohamed Elhoseiny, Marcus Rohrbach, and Tinne Tuytelaars. Memory aware synapses: Learning what (not) to forget. In *Proceedings of the European Conference on Computer Vision (ECCV)*, pages 139–154, 2018.

[3] Dario Amodei, Sundaram Ananthanarayanan, Rishita Anubhai, Jingliang Bai, Eric Battenberg, Carl Case, Jared Casper, Bryan Catanzaro, Qiang Cheng, Guoliang Chen, et al. Deep speech 2: End-to-end speech recognition in english and mandarin. In *Proceedings of the International conference on Machine Learning*, pages 173–182, 2016.

[4] Antreas Antoniou, Massimiliano Patacchiola, Mateusz Ochal, and Amos Storkey. Defining benchmarks for continual few-shot learning, 2020.

[5] Alexei Baevski, Henry Zhou, Abdelrahman Mohamed, and Michael Auli. wav2vec 2.0: A framework for self-supervised learning of speech representations. *arXiv preprint arXiv:2006.11477*, 2020.

[6] Eden Belouadah and Adrian Popescu. Il2m: Class incremental learning with dual memory. In *Proceedings of the IEEE International Conference on Computer Vision*, pages 583–592, 2019.

[7] Francisco M Castro, Manuel J Marín-Jiménez, Nicolás Guil, Cordelia Schmid, and Karteek Alahari. End-to-end incremental learning. In *Proceedings of the European conference on computer vision (ECCV)*, pages 233–248, 2018.

[8] Arslan Chaudhry, Puneet K Dokania, Thalaiyasingam Ajanthan, and Philip HS Torr. Riemannian walk for incremental learning: Understanding forgetting and intransigence. In *Proceedings of the European Conference on Computer Vision (ECCV)*, pages 532–547, 2018.

[9] Arslan Chaudhry, Marc'Aurelio Ranzato, Marcus Rohrbach, and Mohamed Elhoseiny. Efficient lifelong learning with a-gem. In *International Conference on Learning Representations*, 2019.

[10] Arslan Chaudhry, Marcus Rohrbach, Mohamed Elhoseiny, Thalaiyasingam Ajanthan, Puneet K. Dokania, Philip H. S. Torr, and Marc'Aurelio Ranzato. On tiny episodic memories in continual learning, 2019.

[11] Heng-Tze Cheng, Levent Koc, Jeremiah Harmsen, Tal Shaked, Tushar Chandra, Hrishi Aradhye, Glen Anderson, Greg Corrado, Wei Chai, Mustafa Ispir, et al. Wide & deep learning for recommender systems. In *Proceedings of the 1st workshop on deep learning for recommender systems*, pages 7–10, 2016.

[12] Jia Deng, Wei Dong, Richard Socher, Li-Jia Li, Kai Li, and Li Fei-Fei. Imagenet: A large-scale hierarchical image database. In *2009 IEEE conference on computer vision and pattern recognition*, pages 248–255. IEEE, 2009.

[13] Prithviraj Dhar, Rajat Vikram Singh, Kuan-Chuan Peng, Ziyan Wu, and Rama Chellappa. Learning without memorizing. In *Proceedings of the IEEE Conference on Computer Vision and Pattern Recognition*, pages 5138–5146, 2019.

[14] Chrisantha Fernando, Dylan Banarse, Charles Blundell, Yori Zwols, David Ha, Andrei A. Rusu, Alexander Pritzel, and Daan Wierstra. Pathnet: Evolution channels gradient descent in super neural networks, 2017.

[15] Ian J Goodfellow, Mehdi Mirza, Da Xiao, Aaron Courville, and Yoshua Bengio. An empirical investigation of catastrophic forgetting in gradient-based neural networks. *arXiv preprint arXiv:1312.6211*, 2013.

[16] Danijar Hafner, Timothy Lillicrap, Ian Fischer, Ruben Villegas, David Ha, Honglak Lee, and James Davidson. Learning latent dynamics for planning from pixels. In *Proceedings of the International Conference on Machine Learning*, pages 2555–2565. PMLR, 2019.

[17] Kaiming He, Xiangyu Zhang, Shaoqing Ren, and Jian Sun. Deep residual learning for image recognition. In *Proceedings of the IEEE conference on computer vision and pattern recognition*, pages 770–778, 2016.

[18] Xiangnan He, Lizi Liao, Hanwang Zhang, Liqiang Nie, Xia Hu, and Tat-Seng Chua. Neural collaborative filtering. In *Proceedings of the 26th international conference on world wide web*, pages 173–182, 2017.

[19] Sepp Hochreiter and Jürgen Schmidhuber. Long short-term memory. *Neural computation*, 9(8):1735–1780, 1997.

[20] Saihui Hou, Xinyu Pan, Chen Change Loy, Zilei Wang, and Dahua Lin. Learning a unified classifier incrementally via rebalancing. In *Proceedings of the IEEE Conference on Computer Vision and Pattern Recognition*, pages 831–839, 2019.

[21] James Kirkpatrick, Razvan Pascanu, Neil Rabinowitz, Joel Veness, Guillaume Desjardins, Andrei A Rusu, Kieran Milan, John Quan, Tiago Ramalho, Agnieszka Grabska-Barwinska, et al. Overcoming catastrophic forgetting in neural networks. *Proceedings of the national academy of sciences*, 114(13):3521–3526, 2017.

[22] Alex Krizhevsky. Learning multiple layers of features from tiny images. 2009.

[23] Matthias De Lange, Rahaf Aljundi, Marc Masana, Sarah Parisot, Xu Jia, Ales Leonardis, Gregory Slabaugh, and Tinne Tuytelaars. A continual learning survey: Defying forgetting in classification tasks, 2019.

[24] Zhizhong Li and Derek Hoiem. Learning without forgetting. *IEEE transactions on pattern analysis and machine intelligence*, 40(12):2935–2947, 2017.

[25] Vincenzo Lomonaco and Davide Maltoni. Core50: a new dataset and benchmark for continuous object recognition. In *Proceedings of the 1st Annual Conference on Robot Learning*, volume 78, pages 17–26, 2017.

[26] David Lopez-Paz and Marc'Aurelio Ranzato. Gradient episodic memory for continual learning. In *Advances in neural information processing systems*, pages 6467–6476, 2017.

[27] Jie Lu, Anjin Liu, Fan Dong, Feng Gu, Joao Gama, and Guangquan Zhang. Learning under concept drift: A review. *IEEE Transactions on Knowledge and Data Engineering*, page 1–1, 2018.

[28] Ning Lu, Guangquan Zhang, and Jie Lu. Concept drift detection via competence models. *Artificial Intelligence*, 209:11–28, 2014.

[29] Arun Mallya, Dillon Davis, and Svetlana Lazebnik. Piggyback: Adapting a single network to multiple tasks by learning to mask weights. In *Proceedings of the European Conference on Computer Vision (ECCV)*, pages 67–82, 2018.

[30] Arun Mallya and Svetlana Lazebnik. Packnet: Adding multiple tasks to a single network by iterative pruning. In *Proceedings of the IEEE Conference on Computer Vision and Pattern Recognition*, pages 7765–7773, 2018.

[31] Marc Masana, Xialei Liu, Bartlomiej Twardowski, Mikel Menta, Andrew D Bagdanov, and Joost van de Weijer. Class-incremental learning: survey and performance evaluation. *arXiv preprint arXiv:2010.15277*, 2020.

[32] Marc Masana, Tinne Tuytelaars, and Joost van de Weijer. Ternary feature masks: continual learning without any forgetting. *arXiv preprint arXiv:2001.08714*, 2020.

[33] Michael McCloskey and Neal J Cohen. Catastrophic interference in connectionist networks: The sequential learning problem. In *Psychology of learning and motivation*, volume 24, pages 109–165. Elsevier, 1989.

[34] Seyed Iman Mirzadeh, Mehrdad Farajtabar, Razvan Pascanu, and Hassan Ghasemzadeh. Understanding the role of training regimes in continual learning, 2020.

[35] Tom Mitchell, William Cohen, Estevam Hruschka, Partha Talukdar, Bishan Yang, Justin Betteridge, Andrew Carlson, Bhavana Dalvi, Matt Gardner, Bryan Kisiel, et al. Never-ending learning. *Communications of the ACM*, 61(5):103–115, 2018.

[36] Volodymyr Mnih, Koray Kavukcuoglu, David Silver, Andrei A Rusu, Joel Veness, Marc G Bellemare, Alex Graves, Martin Riedmiller, Andreas K Fidjeland, Georg Ostrovski, et al. Human-level control through deep reinforcement learning. *nature*, 518(7540):529–533, 2015.

[37] Jason Ramapuram, Magda Gregorova, and Alexandros Kalousis. Lifelong generative modeling. *arXiv preprint arXiv:1705.09847*, 2017.

[38] Sylvestre-Alvise Rebuffi, Alexander Kolesnikov, Georg Sperl, and Christoph H Lampert. icarl: Incremental classifier and representation learning. In *Proceedings of the IEEE conference on Computer Vision and Pattern Recognition*, pages 2001–2010, 2017.

[39] David Rolnick, Arun Ahuja, Jonathan Schwarz, Timothy Lillicrap, and Gregory Wayne. Experience replay for continual learning. In *Advances in Neural Information Processing Systems*, pages 350–360, 2019.

[40] Amir Rosenfeld and John K Tsotsos. Incremental learning through deep adaptation. *IEEE transactions on pattern analysis and machine intelligence*, 2018.

[41] Shibani Santurkar, Dimitris Tsipras, and Aleksander Madry. Breeds: Benchmarks for subpopulation shift, 2020.

[42] Jeffrey C Schlimmer and Richard H Granger. Incremental learning from noisy data. *Machine learning*, 1(3):317–354, 1986.

[43] Joan Serra, Didac Suris, Marius Miron, and Alexandros Karatzoglou. Overcoming catastrophic forgetting with hard attention to the task. *arXiv preprint arXiv:1801.01423*, 2018.

[44] David Silver, Julian Schrittwieser, Karen Simonyan, Ioannis Antonoglou, Aja Huang, Arthur Guez, Thomas Hubert, Lucas Baker, Matthew Lai, Adrian Bolton, et al. Mastering the game of go without human knowledge. *nature*, 550(7676):354–359, 2017.

[45] Shagun Sodhani, Sarath Chandar, and Yoshua Bengio. Toward training recurrent neural networks for lifelong learning. *Neural computation*, 32(1):1–35, 2020.

[46] Mohammad Sorower. A literature survey on algorithms for multi-label learning.

[47] Sebastian Thrun and Tom M. Mitchel. Lifelong robot learning. *Robotics and Autonomous Systems*, 1995.

[48] Sebastian Thrun and Tom M. Mitchel. Child: A first step towards continual learning. *Machine Learning*, 28:77–104, 1997.

[49] Gido M. van de Ven and Andreas S. Tolias. Three scenarios for continual learning. In *Neurips 2018*, 2018.

[50] Ashish Vaswani, Noam Shazeer, Niki Parmar, Jakob Uszkoreit, Llion Jones, Aidan N Gomez, Łukasz Kaiser, and Illia Polosukhin. Attention is all you need. In *Advances in neural information processing systems*, pages 5998–6008, 2017.

[51] Yue Wu, Yinpeng Chen, Lijuan Wang, Yuancheng Ye, Zicheng Liu, Yandong Guo, and Yun Fu. Large scale incremental learning. In *Proceedings of the IEEE Conference on Computer Vision and Pattern Recognition*, pages 374–382, 2019.

[52] Friedemann Zenke, Ben Poole, and Surya Ganguli. Continual learning through synaptic intelligence. In *Proceedings of the International conference on Machine Learning*, volume 70, pages 3987–3995. PMLR, 2017.